Persistent fine-scale fault structure and rupture development: A new twist in the Parkfield, California, story

Clément Perrin [a,b,*], Felix Waldhauser [a], Eunseo Choi [c], Christopher H. Scholz [a]

[a] *Lamont Doherty Earth Observatory at Columbia University, New York, USA*
[b] *Université de Paris, Institut de Physique du Globe de Paris, CNRS, F-75005 Paris, France*
[c] *Center for Earthquake Research and Information, University of Memphis, 3890 Central Ave., Memphis, TN, 38152, USA*

A B S T R A C T

We investigate the fine-scale geometry and structure of the San Andreas Fault near Parkfield, CA, and their role in the development of the 1966 and 2004 ∼M6 earthquakes. Long-term surface fault traces indicate that structural heterogeneities associated with secondary reverse and normal fault structures are present at both rupture tips, near Middle Mountain and Gold Hill. Detailed analysis of almost 50 years of high-resolution seismicity reveals a fault plane that has been twisted into a helicoid between Middle Mountain and Gold Hill. Numerical models support our conclusion that this shape is the result of long-term torqueing of a strong stuck patch surrounded by a weak creeping region. The changes in fault friction behavior and related geometric discontinuities act as barriers to rupture propagation of moderate size earthquakes at Parkfield, and as areas of concentrations where rupture initiates. Our study demonstrates also that smooth strike-slip faults with large cumulative offset can form new fault segments at a late stage in their evolution.

© 2019 Elsevier B.V. All rights reserved.

1. Introduction

The Parkfield section of the San Andreas fault is one of the best-instrumented earthquake source region in the world. Over the past 50 years, one and a half seismic cycles, including two M∼6 earthquakes in 1966 and 2004, have been observed there with full geodetic and seismic coverage. Yet it is still unclear how the earthquake generation process takes place in this peculiar area. It has long been recognized that the M∼6 earthquakes break a stuck patch imbedded in an otherwise creeping fault – first noted by Harris and Segall (1987) and most recently modeled by Barbot et al. (2012). It has also been observed that the rupture zone lies between two geometrical discontinuities in the fault, a slight compressional bend in the north near Middle Mountain (MM) and an extensional jog in the south near Gold Hill (GH) (Lindh and Boore, 1981). Neither the connection between these features nor their role in the nucleation and termination of the M∼6 earthquake ruptures have been elucidated.

The 1966 earthquake initiated at the northern end of the rupture area near Middle Mountain, propagated unilaterally to the southeast along the entire Parkfield section and stopped near Cholame (CH) (Figs. 1 and 2; Brown et al., 1967; McEvilly et al., 1967). In contrast, the 2004 earthquake initiated in the south near Gold-Hill (GH), then propagated mainly to the northwest and stopped near MM (Figs. 1 and 2; Langbein et al., 2005; Rymer et al., 2006). Both surface ruptures were similar, formed by small fractures associated with local displacements less than 0.1 m (Brown et al., 1967; Rymer et al., 2006). Source inversion models of the 2004 event reveal two main slip patches close to either end of the rupture extent, with maximum slip ranging from 0.5 to 1 m (see an example in Fig. 3), followed by post-seismic afterslip near the surface above the coseismic rupture zone (e.g., Barbot et al., 2009; Johanson et al., 2006; Langbein et al., 2006; Murray and Langbein, 2006) but also at depth in the lower crust (Bruhat et al., 2011). Similar co-seismic distribution associated with shallow postseismic behavior has been observed for the 1966 earthquake (see an example in Fig. 3; e.g. Archuleta and Day, 1980; Scholz et al., 1969; Segall and Du, 1993).

In order to better understand rupture initiation, propagation and arrest of the two latest M6 earthquakes at Parkfield, we present here a combined analysis of high-resolution near surface and earthquake data that image the fine-scale structures of the San Andreas Fault. We bring together geologic fault information available in the literature and a broad range of satellite images and topographic data to refine the long-term surface fault traces along the Parkfield section. We also compute high-resolution

* Corresponding author at: Université de Paris, Institut de Physique du Globe de Paris, CNRS, F-75005 Paris, France.
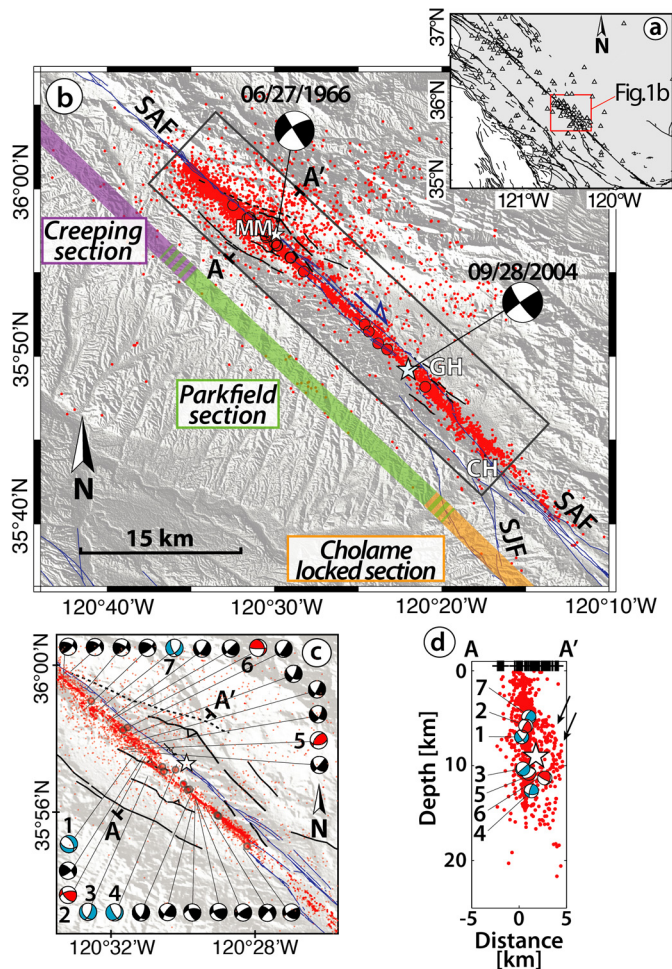*E-mail address:* perrin@ipgp.fr (C. Perrin).

Fig. 1. a) Map view of central California. White triangles are the 212 stations that recorded the ~17,000 events; b) Fault map along the Parkfield section and relocated seismicity (red dots) from 1966 to 2015. Black circles are events with M ≥ 4. White stars are the 1966 and 2004 epicenters. Fault traces are shown on SRTM3 topography illuminated from the southwest. Blue lines are quaternary fault traces from the (U.S. Geological Survey and California Geological Survey, 2006); black lines are additional long-term fault traces from this study and Thayer (2006) (dotted black lines when uncertain). SAF: San Andreas Fault; SJF: San Juan Fault; MM: Middle Mountain; GH: Gold Hill; CH: Cholame; c) Zoom into Middle Mountain area. Focal mechanisms (Hardebeck, 2010) showing intermediate to low-angle dipping fault motions (<70°). d) Cross section (AA′) showing the relocated seismicity from 1966 to 2015 (red dots) at Middle Mountain. Black crosses are fault traces at surface. The white star represents the 1966 hypocenter. Black arrows point possible secondary active strands at depth. Numbered focal mechanisms in c) and d) point out specific thrust (red) and normal (blue) faulting earthquakes (front projection). (For interpretation of the colors in the figure(s), the reader is referred to the web version of this article.)

seismicity recorded at the Northern California Seismic Network (NCSN) between 1969 and 2015, and aftershocks recorded during the 2 months following the 1966 earthquake (Eaton et al., 1970), spanning a nearly 50 year time period including two ~M6 events. Using these new data, we relate the structures observed at the surface to persistent deformation patterns along the three-dimensional fault plane at depth. Supported by numerical simulations of the long-term fault deformation, we propose a new mechanical model for the Parkfield segment of the San Andreas fault that differs from previous studies (e.g., Simpson et al., 2006).

2. Data analysis and results

2.1. Surface fault traces

According to the quaternary surface fault map from the USGS (U.S. Geological Survey and California Geological Survey, 2006);

blue lines Figs. 1b and 1c), the ~30 km long Parkfield section is composed of two linear, roughly N139°E striking, sub-parallel strands (also called the main San Andreas fault and the southwest fracture zone) that join each other at both terminations of the Parkfield section through two structural complexities: i) at the southern end near GH, an extensional jog, where the fault trace bends twice with deviations up to 28° from the mean fault strike (GH-CH, Figs. 1b and 2c); ii) at the northern end, near MM, a 5° restraining bend (Lindh and Boore, 1981) (MM, Figs. 1b and 2c).

We analyzed multi-resolution satellite images (Google Earth, Landsat 7) and topographic data (SRTM 30 m, LiDAR available from opentopography.org) and identified additional structural features (black lines in Figs. 1b and 1c): around MM, the active fault trace is surrounded by multiple secondary faults several kilometers away from the main San Andreas Fault and clearly imprinted in the topography (Fig. 1c). Most of them have been previously recognized as secondary strike-slip and reverse faults in the field (Thayer, 2006). Altogether they contribute to forming the localized relief observed at the center of the main fault trace. The overall shape of this structural feature, which encompasses an area approximately 5 km wide and 10 km long, resembles a restraining step-over feature that separates the locked Parkfield section from the creeping section. These secondary faults strike between N110°E and N150°E, in good agreement with earthquake locations derived in this study and focal mechanisms from Hardebeck (2010) that show oblique reverse and normal faulting (Fig. 1c; see also Thurber et al., 2006). The 1966 and 2004 earthquakes initiated and stopped near these large structural discontinuities observed at the surface near GH-CH and MM.

2.2. Earthquake relocation

We use seismicity data to investigate the depth extent of the heterogeneities observed near the surface. We first apply a 3D grid search method (*NLLoc* program; Lomax et al., 2000) to determine new absolute locations of more than ~17,000 earthquakes from 1966–2015 in the 3D velocity model of Thurber et al. (2006). The strike of the new 3D absolute locations is rotated slightly (up to ~2°) counterclockwise compared to the original NCSN locations as a result of properly accounting for the velocity variations across the fault zone. We then use the double-difference algorithm *HypoDD* (Waldhauser, 2001; Waldhauser and Ellsworth, 2000) to compute precise relative locations using both travel-time differences from P-wave pick data (available from 1966 to 2015) and P- and S-wave cross correlation delay time data (1984–2015) (Schaff and Waldhauser, 2005). We included all events with at least 4 stations in order to be able to simultaneously relocate the aftershocks of the 1966 earthquake (Eaton et al., 1970) together with the rest of the seismicity. The resulting locations are shown in Fig. 1, S1c and S1d. These locations resolve the fine shape of the fault plane at a level of a few tens of meters. The median lateral relative error at the 95% confidence level, derived from a bootstrap analysis of the fine residuals, is 0.039 km and the median vertical relative error is 0.022 km (Fig. S2).

Most events with M < 1 (M_L is considered for events M > 3, M_D for smaller events; see Uhrhammer et al., 2011) are located in the creeping section (see Supplementary Figs. S1a and S1b). A cross-section at MM (Fig. 1d) indicates that some events also delineate secondary oblique strands in the eastern part (see black arrows) that connect to the main fault at ~10 and ~12 km depth, close to the 1966 nucleation area. Several reverse and normal faulting focal mechanisms located between 10 and 15 km deep (events 3, 4, 5 and 6 in Figs. 1c and 1d) are aligned with those secondary strands, while those located between 0 and 10 km deep (events 1, 2 and 7 in Figs. 1c and 1d), appear to be re-
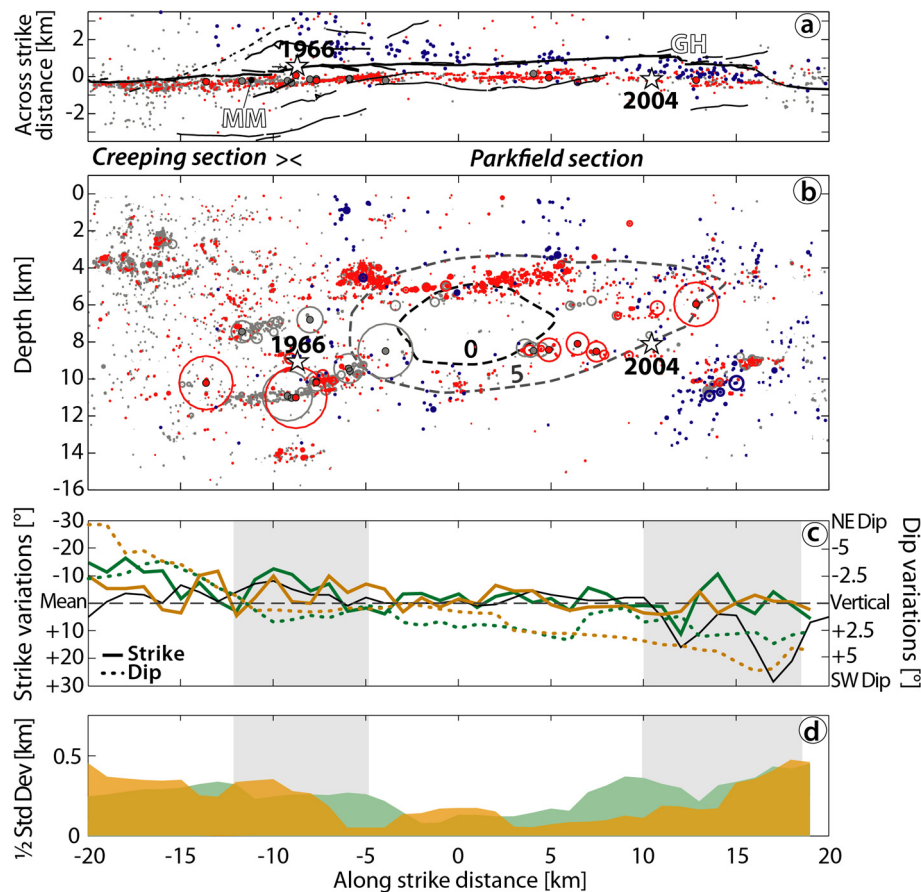
Fig. 2. a) Rotated map view of all surface fault traces from Fig. 1 (black lines) and the relocated seismicity (M ≥ 1). Blue and red dots are early aftershocks (2 months) of the 1966 and 2004 ~M6 earthquakes, respectively. Gray dots are background seismicity (1984 to 2015; see Supplementary Fig. S1 for full catalog). Larger dots are M ≥ 4 events since 1979. White stars represent the 1966 and 2004 epicenters. MM: Middle Mountain; GH: Gold Hill. b) Along-strike cross section. Same legend as in a. Circles indicate size of a circular source model with a 3 MPa stress drop. Dashed dark lines are contours of the interseismic slip rate in mm/yr predicted by geodetic inversion (Harris and Segall, 1987). c) Variation of the fault strike and dip along the Parkfield section. The mean reference fault strike and dip are 139° and 90° (vertical), respectively. Solid black curve represents the main San Andreas fault strike measured at surface (secondary faults not included). Green and orange curves are inferred strike and dip at depth from the best fitting planes for the 1984–2004 and 2004–2015 interseismic periods, respectively. Gray zones are location of major complexities observed at surface near Middle Mountain and Gold Hill-Cholame. d) Half standard deviation from the best fitting planes calculated in each box (see also Supplementary Figs. S4 and S5) for the 1984–2004 and 2004–2015 interseismic periods (green and orange shaded curves, respectively).

lated to the secondary fault traces observed at the surface (black crosses, Fig. 1d).

2.2.1. Distribution of the 1966 and 2004 aftershocks

In the following analysis, we only consider earthquakes of M ≥ 1, corresponding to the minimum magnitude of completeness of the earthquake catalog (see Supplementary Fig. S3). Fig. 2 shows the distribution of the 1966 and 2004 aftershocks within 2 months of the mainshock (in blue and red, respectively). The along strike distribution of the aftershocks is sharp and fairly similar for both events, mostly situated between 4 and 12 km deep along the Parkfield section. Distinctive seismicity patches (e.g. streaks, clusters, repeating events, Waldhauser et al., 2004; Thurber et al., 2006) outline an area devoid of earthquakes between 6–9 km deep, corresponding to the main locked patch of the fault that broke in the 1966 and 2004 events (dashed lines in Fig. 2b, Harris and Segall, 1987). The 1966 and 2004 aftershock sequences are similarly distributed, especially near GH-CH where two distinct patches of seismicity, at ~5 km and ~10 km depth, are superimposed (Fig. 2b), suggesting that the same main fault strand has been activated during the two earthquakes. A high concentration of number of aftershocks (including all M ≥ 4 events) and cumulative moment release are observed near the rupture tips of the 1966 and 2004 earthquakes (Fig. 2a, b; Fig. 3a, b).

We note that in the northwestern part of the Parkfield section, the 1966 aftershocks tend to deviate further to the northeast away from the San Andreas fault trace (blue dots in map view on Fig. 2a). This deviation is also observed in the original absolute locations and might be due to the poor station coverage in the northwestern part of the 1966 rupture zone (Eaton et al., 1970). However, few events are concerned and our relocations are in good agreement with previous studies in the southeastern part of the Parkfield section, where most of the seismicity is localized (Fig. 2; e.g., Thurber et al., 2006; Waldhauser and Schaff, 2008). More generally, less than 20 permanent and temporary stations recorded aftershock activity following the 1966 earthquake, with several periods of interrupted service (Eaton et al., 1970). This likely explains why the aftershock activity and the cumulative seismic moment release shown in Fig. 3 are much lower for the 1966 sequence compared to the one in 2004.

2.2.2. Interseismic periods 1969–2004 and 2005–2015

We choose to represent in Fig. 2 only the best (i.e., correlation based) relocations (gray dots) for the two interseismic periods from 1984–2004 and 2005–2015 for a fine-scale representation of the geometrical features (see Supplementary Fig. S1 for the entire relocated catalog). The interseismic seismicity distribution is remarkably similar to the co- and postseismic distributions. Fig. 3 shows along strike cross sections of the earthquake density and
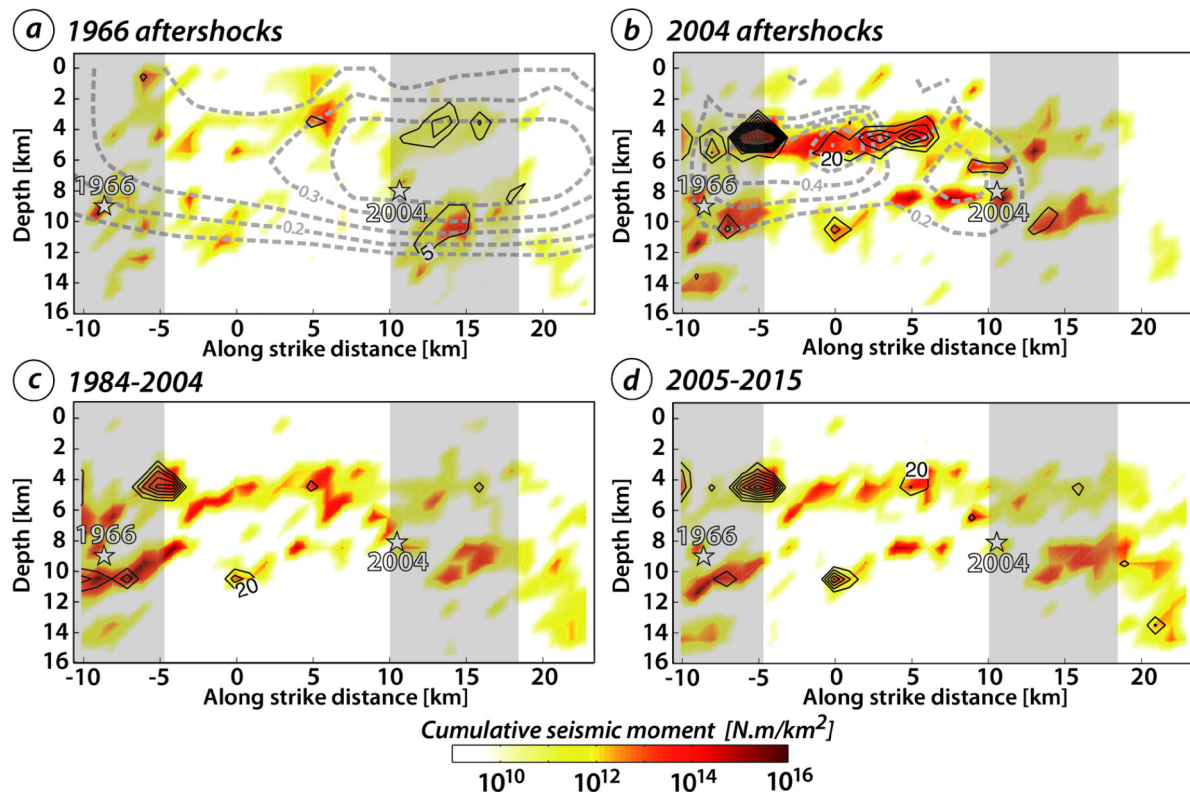
Fig. 3. Along-strike cross-sections showing projected earthquake density (contours, counts per km^2) and cumulative seismic moment (color scale) released along the Parkfield section for a) 1966 and b) 2004 aftershocks, and c) 1984–2004 and d) 2005–2015 periods. White stars are 1966 and 2004 ∼M6 hypocenters. Grey dashed lines are coseismic slip distributions (in m) of the a) 1966 (Segall and Du, 1993) and b) 2004 (Bruhat et al., 2011) earthquakes. Gray zones are location of major complexities observed at surface near Middle Mountain and Gold Hill-Cholame.

cumulative seismic moment released within 2 months after the 1966 and 2004 Parkfield earthquakes (Figs. 3a and 3b, respectively), and during the 1984–2004 and 2005–2015 interseismic periods (Figs. 3c and 3d, respectively). Density contour lines point out five, possibly six, persistent kilometer scale seismicity patches during the interseismic periods (Figs. 3c and 3d). A patch of higher density is located at the northern end of the Parkfield section at 4 km depth, a patch that was also activated by aftershocks of the 2004 event (Fig. 3b).

The interseismic, cumulative moment release maps allow us to distinguish other patches which are lining up at 4–6 km and ∼10 km depth (Figs. 3c and 3d), again in good agreement with patches that were active during the 1966 and 2004 post seismic periods (Figs. 3a and 3b).

2.2.3. 3D fault geometry

We determine the three-dimensional fault geometry by applying a principal component analysis to all events within 3 × 3 km wide boxes (in map view), stepping at 1 km intervals along the fault trace. For each box, we calculate strike and dip of the plane that minimizes the distance between hypocenters and fault surface during each of two interseismic periods (1984–2004 and 2005–2015) in an attempt to capture the long-term signature of the fault geometry (Fig. 2c). For simplicity, we assume, in each box, a constant dip of the calculated plane. The calculated strike and dip values are presented in Fig. 2c, while an animated view of the data and the combination of the best fitting planes is shown in Supplementary Fig. S6.

The strike measurements show that the strike along the main-shock rupture zone, which includes the stuck patch, is fairly constant, while it deviates from that trend at both ends: the strongest deviations range from N125°E to N150°E (at MM and GH), consistent with surface measurements (see black line in Fig. 2c), albeit

with fluctuating amplitudes. The overall strike variations are also in good agreement with focal mechanisms derived by Hardebeck (2010; Supplementary Fig. S7). Fig. 2d shows the standard deviations of the seismicity from the best fitting planes for each interseismic periods, characterizing the normal distance of the events from the best fitting planes (see also Supplementary Figs. S4 and S5 for detailed event distribution). It confirms that MM and GH-CH are characterized by greater deviations of hypocenters from the plane (400–500 m), suggesting a wider off-fault deformation zone, compared to the Parkfield section (100–200 m). The systematic variation in strike along the fault indicates a twist in the fault plane along a vertical axis.

Furthermore, the fault dip varies steadily from northeast dipping in the north to southwest dipping in the south, indicating a twist in the fault plane along a horizontal axis (Fig. 2c; e.g. Kim et al., 2016). The 3D fault geometry of the San Andreas fault at Parkfield can thus be best described as a helicoid (Supplementary Fig. S6). The change in fault dip from northwest to southeast can also be observed in the original NCSN locations, as well as the 3D grid-search absolute locations, indicating that the twist is not an artifact of the relocation procedure or the model used to locate the events (see Supplementary Fig. S8).

Because the seismicity patches are well defined and aligned, we used the principal component analysis to minimize the orthogonal hypocenter distances to a single fault plane in each box (Supplementary Fig. S4). However, we also tried to investigate the possibility of multiple fault strands or variations of the fault dip at depth below and above 7 km (i.e. the limit between the main patches of seismicity; see Supplementary Fig. S4). The resulting fault planes were poorly constrained, especially the dip values, because their fits were mostly controlled by single sub-horizontal streaks, rather than events well distributed on a plane in three-dimensional space. Estimating an orientation by fitting one single plane in each box
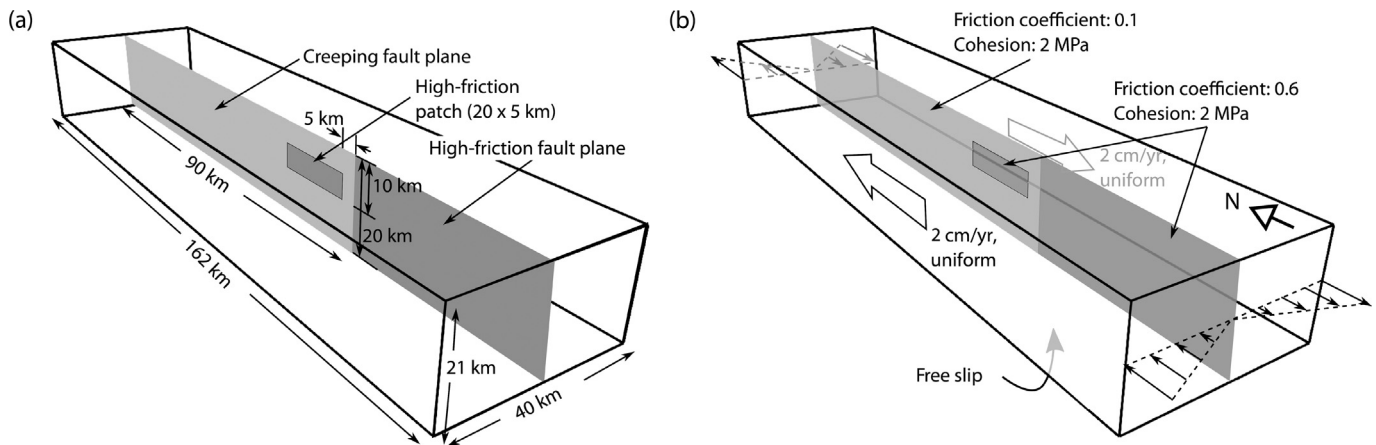
Fig. 4. (a) Geometry of the model domain and the fault plane. (b) Boundary conditions on the sides and the bottom as well as frictional properties on the fault plane. The top surface is a free surface. The fault section of the model includes creeping sections (in grey) and fully locked zone (in white; stuck patch near Parkfield and Southern Cholame/Fort Tejon section).

tend to smooth local irregularities that might be due to multiple fault strands at depth. Event distributions away from the fault planes (Supplementary Fig. S5) show that the Parkfield section is mainly characterized by a clear and sharp single strand of ∼100 m wide. Secondary peaks, indicating possible oblique secondary strands, are observed around MM and GH-CH. Therefore, our approach cannot describe in detail the complexity of the damage zone around the fault core, but it allows us to highlight significant discontinuities with great confidence.

3. Numerical model of the effect of a strong stuck patch on fault geometry

The creeping section is known from studies at SAFOD to be very weak, with a friction coefficient μ ∼0.15 due to the presence of weak phyllosilicates in the fault zone (i.e. saponite at shallower depth, Carpenter et al., 2015; Lockner et al., 2011, to talc below 3 km deep, Moore et al., 2016). They appear to be produced by reaction between the serpentinite of the Coast Ranges ophiolite and the silicious rocks of the Salinian block (Moore and Lockner, 2013) – a geologic context that is only present along the creeping section (Allen, 1968; Irwin and Barnes, 1975). On the other hand, the stuck patch at Parkfield cannot be lined with weak phyllosilicates because they are velocity strengthening and will not facilitate seismic instability. The only possible materials that can be velocity weakening and exhibit the frictional strength of the stuck patch in this area are granite, antigorite or lizardite forms of serpentinite (Moore and Rymer, 2007). These all have high strength with friction coefficients between 0.5–0.75. Thus, the seismogenic stuck patch has a higher friction coefficient than the surrounding creeping segment and thus can sustain greater shear stress than the stress-drops observed in Parkfield earthquakes (on the order of ∼1 MPa). Since the earthquakes do not relieve all the stresses on the stuck patch, there must be a permanent torque produced by that high-stress patch surrounded by low stress regions. As a result, over time periods longer than the seismic cycle, slow inelastic deformation will occur in response to this torque and the twist in the fault plane will develop.

In the following section, we present a numerical model that supports the above idea. Rather than simulate the entire process of accumulating torque and inelastic deformations, we focus on showing that a high-friction patch embedded in a low-friction fault plane, representing the stuck patch situation, is able to generate deformations that are consistent with the proposed helicoidal twisting of the fault plane.

3.1. Model setup

We use PyLith, a portable, scalable finite element software for simulation of crustal deformation and earthquake faulting (Aagaard et al., 2016, 2013), to simulate the deformation of linear elastic crust containing a straight strike-slip fault with heterogeneous frictional strengths. The model domain, covering an area 40 × 162 km wide and 21 km-thick (Fig. 4a), is discretized into hexahedral linear elements with edge length of 1 to 1.5 km. Density of the crust is assumed to be 2500 kg/m³ and Vs and Vp to be 3 and 5.2915 km/s. These values are equivalent to shear and bulk modulus of 22.5 and 55 GPa, respectively. Completely contained within the crust, the modeled zero-thickness fault plane is 90 km long and 20 km tall, going through the center of the domain parallel to the longest edge of the domain. The creeping section is represented by a low-friction section with a uniform friction coefficient of 0.1 and a cohesion of 2 MPa ("creeping fault plane" in Fig. 4a). The stuck patch is modeled as a simplified rectangular zone of 20 × 5 km ("high friction patch" in Fig. 4; Harris and Segall, 1987). It has a uniform friction coefficient of 0.6 and a cohesion of 2 MPa. The fault section that broke during the 1857 earthquake ("high-friction fault plane" in Fig. 4), is considered to have the same friction coefficient and cohesion as the stuck patch. All the fault sections are allowed to slip because we model fault behaviors for a time period corresponding to multiple earthquake cycles, over which no part of the Parkfield section would remain completely locked.

Right-lateral motion at a rate of 2 cm/yr on two fault-parallel domain boundaries (relative on-fault slip rate of 4 cm/yr) with the normal component of velocity (v_x) set to be zero and the vertical component (v_z) free (Fig. 4b). On the fault-perpendicular sides, a simple-shear velocity field is applied such that the strike-parallel component varies between +2 and −2 cm/yr linearly with distance across the fault. The fault perpendicular component is set to be zero and the vertical component is free on these boundaries. The bottom boundary is a free-slip surface. The top boundary is a free surface with zero traction. The effect of gravity is considered and the initial stress is set to be lithostatic.

We get fault displacements and stresses as a response to incrementally increasing amounts of boundary displacements. Although we apply velocities to generate strike-slip kinematics, the velocity boundary conditions are simply a way of increasing strike-slip motions incrementally at each time step. Our models simulate only linear elastic behaviors of rocks and does not directly show rate-dependent effects. Nonetheless, the correspondence principle (e.g., Sec. 2.5.7, LeMaitre, 2001) ensure the relevance to permanent helicoidal twisting of the Parkfield section. According to this principle,
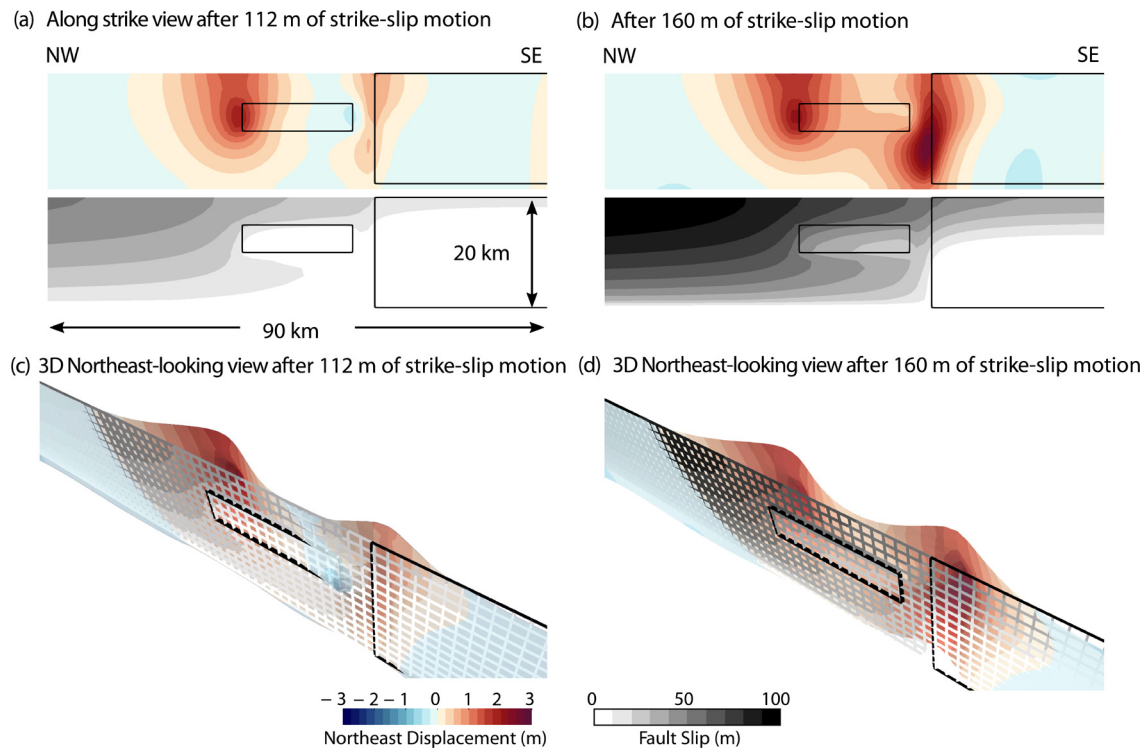
(a) Along strike view after 112 m of strike-slip motion   (b) After 160 m of strike-slip motion

(c) 3D Northeast-looking view after 112 m of strike-slip motion   (d) 3D Northeast-looking view after 160 m of strike-slip motion

Fig. 5. (a) Perpendicular displacement of the fault plane toward the northeast and slightly toward the southwest (top) and cumulative fault slip distribution (bottom) around the stuck patch and the high-friction section outlined by the solid black rectangles after 112 m of boundary displacement. (b) Same as in (a) after 160 m of boundary displacement. (c) and (d) Northeast-looking view of the fault plane after 112 m and 160 m of boundary displacement, respectively (mesh with the slip magnitudes colored in gray scale), and the central plane deformed by the northeast and southwest directed displacements. The solid back rectangles outline the stuck patch and the high-friction section.

strain rate field in a linear viscoelastic model would be equivalent to elastic strain field in the corresponding linear elastic model under the same boundary conditions. So, we can view our model's strain field as a strain rate field for long term deformation.

3.2. Results

Fig. 5 presents the northeastern displacements on the fault plane when the high-friction patch and the upper 2 km of the high-friction plane started slipping after 112 m of cumulative displacement (Figs. 5a and 5c). After an unspecifiable number of earthquake cycles, slip would accumulate on the high-friction patch as well. Thus, we also look at the northeastern displacements when the entire high-friction patch as well as the upper 5 km of the high-friction plane has slipped after 160 m of boundary displacement (Figs. 5b and 5d). Relative to the state in Figs. 5a and 5c, northeastern displacements have increased at the northern tip and more at the southern tip of the patch. A major warp of the fault plane occurs at the northern tip of the high-friction patch, corresponding to MM, with northeastern displacements > 1 m along a zone approximately 10 km long (Figs. 5a and 5c). We note also that a section of the fault situated in the southern tip of the stuck patch is slightly displaced toward the southwest when most of the high-friction patch is locked (Figs. 5a and 5c), accentuating the general warp of the fault plane. When the high friction patch starts to slip, the whole section is progressively shifted toward the northeast, but the general warping of the fault plane is still preserved (Figs. 5b and 5d). An animated view of the model is available in the Supplementary material (see Supplementary Fig. S9).

Cross sections in Fig. 6 show the deformation of the San Andreas Fault plane at specific locations along the model (Fig. 6a) after the stuck patch has been fully mobilized (i.e., the stage in Figs. 5b and 5d). The vertical cross-section at MM (Fig. 6b) indi-

cates a northeastern displacement of the fault plane from its original location near the surface (hence a southwest dipping fault). Most of the deformation diffused in the crustal medium is fairly symmetrical relative to the fault plane. It seems to root at the base of the stuck patch and to widen towards the surface in a flower-like structure. The deformation is less pronounced at the southern tip of the stuck patch (i.e., GH, Fig. 6c). Yet, we can distinguish a slight deflection of the fault plane, which is displaced toward the northeast in the shallower and deeper part of the model (i.e. the creeping zones) and less so in an area that corresponds to the stuck patch. Thus, the dip of the fault plane changes with depth (i.e. toward the southwest, northeast and southwest). Fig. 6d is a horizontal cross-section situated at 7.5 km depth, crossing through the creeping zones and the stuck patch (see Fig. 6a). It highlights the variation of the fault strike (grey dotted line) compared to a referenced linear fault direction (black dotted line), in the same way as in Fig. 2d. As shown in Fig. 5, the fault plane is mostly deformed toward the northeast at MM and GH, and much less so in the southern half part of the stuck patch. The strike variations within the stuck patch are consistent with the clockwise rotation of the stuck patch inferred from the seismic data (Figs. 2c, 2d).

Fig. 7 provides additional information on on-fault stress distribution at two stages: after 112 m of displacement (Fig. 7a), the maximum shear stress (∼100 MPa) occurs at the left (northwestern) tip and corners of the rectangular stuck patch (corresponding to MM), which begins to slip. At this point, slip along the stuck patch, which is meant to represent cumulative slip from repeated earthquakes, is about 30 cm with a stress drop of ∼1 MPa, which is regained in ∼30 yrs. Yet, after 160 m of cumulative displacement, stress remains at about 100 MPa throughout the seismic cycles, even after the high-friction patch has slipped (Fig. 7b). Thus, slow anelastic processes can produce permanent deformation of the same type as the elastic ones shown in Fig. 5. This result indicates that the high-friction patch can uphold a higher level of
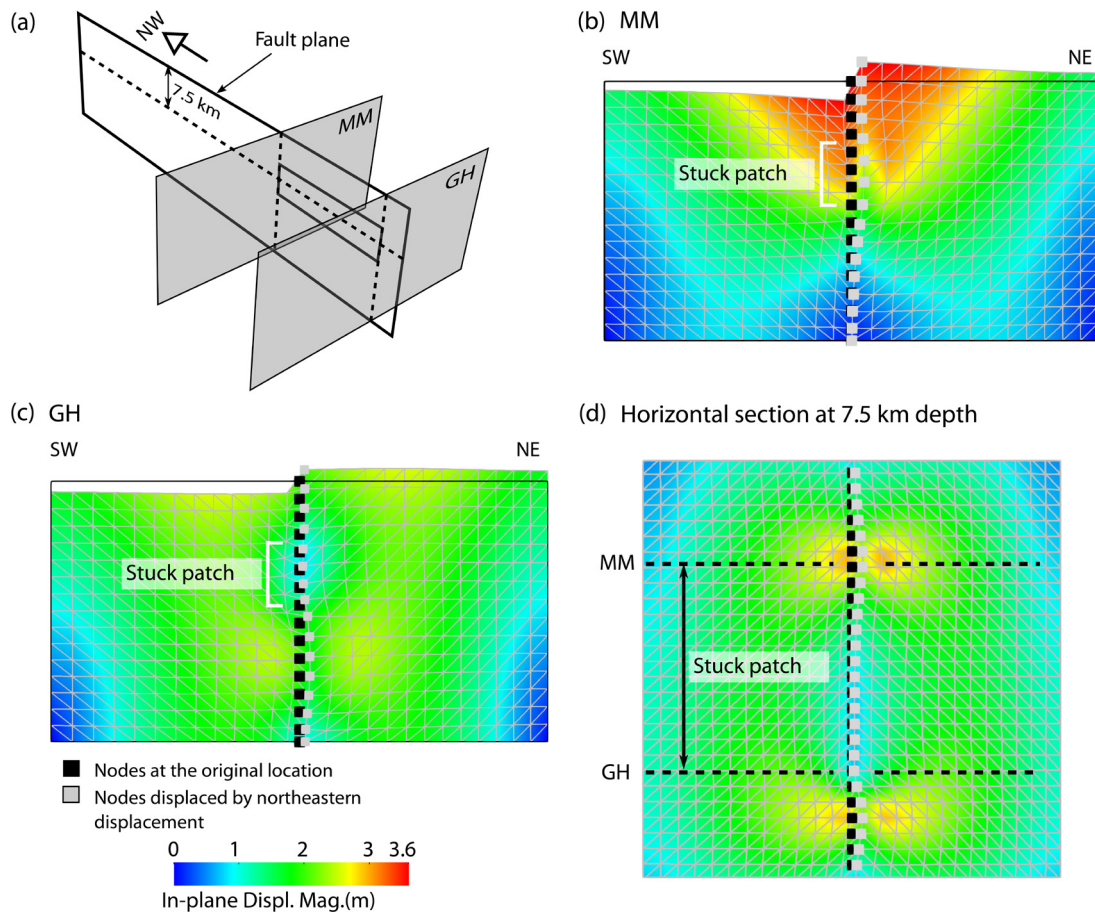
Fig. 6. (a) Locations of the two vertical cross-sections corresponding to Middle Mountain (MM) and Gold Hill (GH) and one horizontal section going through the center of the stuck patch at the depth of 7.5 km. (b) In-plane displacement magnitudes on the MM cross-section that is displaced by the 500 times amplified in-plane displacement vectors. Black squares are the original locations of the nodes on the central plane and gray squares are the displaced locations of the same nodes after 60 m of boundary displacement. Gray lines show the computational mesh. Thin black lines outline the original rectangular shape of the cross-section. (c) Same as (b) but for the GH cross-section. (d) Northeast displacement magnitudes plotted on the horizontal section displaced by the northeast displacement vectors. Symbols are the same as in (b).
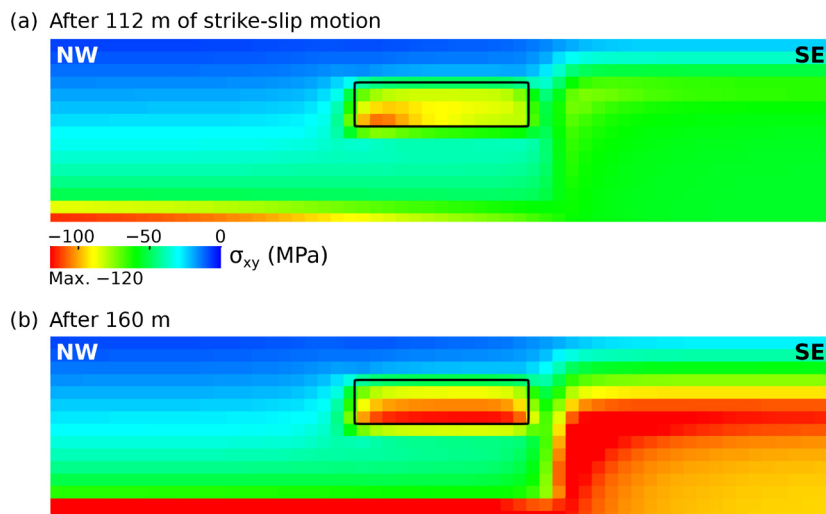

Fig. 7. Along-strike shear stress map on the fault plane at two stages of the simulation (after 112 and 160 m of displacement). Note the x axis is into the plane and the y axis is pointing to the left. So, the right-lateral motion generates negative values of shear stress (σ_{xy}).

stress than the surrounding creeping section permanently, i.e., over a long time period corresponding to many earthquake cycles. In both states, accumulating slip on the creeping section generates high shear stress near the clamped bottom edge of the fault plane. Likewise, shear stress is concentrated right beneath the slipping region on the high-friction section, southeast of the patch (Fig. 7b).

Profiles of shear and normal stresses (σ_{xy} and σ_{xx}, respectively) are shown in Supplementary Fig. S10. Along dip, the shear stress increases on the stuck patch relative to the surrounding creeping regions and higher stress concentrations are localized at the lower part of the stuck patch. Along strike, the variation of shear and normal stresses are consistent with compression at the left tip (MM)
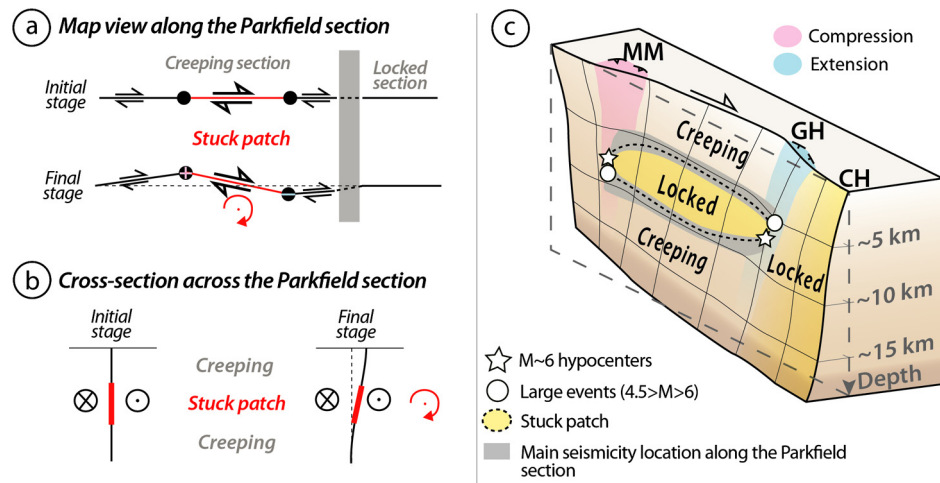
Fig. 8. Schematic map view (a) and cross section (b) showing the clockwise rotation of the fault plane due to the presence of a stuck patch surrounded by a creeping zone. In (a) the size of the shear couple arrows scales with the amount of shear stress. Positive and minus signs are compressional and extensional regimes, respectively; in (b) the increasing size of dextral motion indicates increasing shearing stresses with depth and thus the clockwise torque (red arrows); c) 3D sketch synthesizing the clockwise twist into a helicoidal fault plane at Parkfield and its relation with changes in fault-slip behavior, structural discontinuities and earthquake distribution; MM: Middle Mountain; GH: Gold Hill; CH: Cholame.

and extension at the right tip (GH-CH) of the stuck patch, resulting in clockwise rotation.

4. Discussion

4.1. Progressive deformation of the San Andreas fault over the long-term

4.1.1. Shear stress and friction contrast at the origin of the twist

Our observational results show that the San Andreas fault plane within the rupture region of the recent ∼M6 events has been deformed into a helicoidal surface that extends from the compressional bend at MM in the north to the extensional jog near GH in the south (Fig. 2c and Supplementary Fig. S6). It connects the northern part of the fault to the Cholame section in the south through a ∼2 km wide step. By incorporating changes in fault-slip behavior at depth, our numerical model (Fig. 6) reproduces this twist and thus the variation of the fault strike (Fig. 2d, 6d) and fault dip (Figs. 2d, 6b, 6c) deduced from the seismicity analysis. The stuck patch is stronger than the surrounding creeping areas by a factor of ∼4 (see section 3). The contrasting high right-lateral shear stresses on the patch will induce a torque that will bend the stuck section of the fault clockwise, as shown in Fig. 8a (map view). Because the shear stresses increase with depth, another torque increases the clockwise bending with depth (Fig. 8b). In our numerical model, the increase in shear stress from the surface to 10 km depth is about 30 MPa in the creeping section away from the stuck patch (Fig. 7a, b). However, a much stronger torque is resulted, about 120 MPa over the same vertical distance, through the stuck patch (Fig. 7b). This result shows how the assumed contrast in frictional strength can be responsible for the torques localized around the stuck patch. The two mechanisms in Fig. 8a and Fig. 8b would produce the helicoidal fault geometry that we observe (Fig. 8c). This deformed section acts like a hinge and gate, with the hinge in the north marked by the compressional bend at its onset (MM in pink, Fig. 8c), and the open end of the gate to the south, where it is accommodated by the extensional jog (GH-CH in blue, Fig. 8c). This suggests that the geometrical complexities at the ends of the stuck patch result from the contrast of strength of the stuck patch with the surrounding creeping section of the fault.

4.1.2. Formation and evolution of geometrical complexities and secondary structures

One hypothesis would consider that the geometrical complexities are inherited structures formed before the presence of the

stuck patch in the geologic evolution of the San Andreas fault. They would correspond to ancient relay zones between fault segments, where many WNW-ESE long-term secondary structures (Fig. 1c) would be connected to the main San Andreas Fault. As such they could play an important role in the fault structure and the rupture development of ∼M6 Parkfield earthquakes. They would contribute to control the extent of the rupture, acting as structural barriers (e.g., Biasi and Wesnousky, 2017; Manighetti et al., 2007; Stirling et al., 1996) and places where stress concentrations might also favor rupture initiation (e.g., Aki, 1979; Barka and Kadinsky-Cade, 1988; Manighetti et al., 2015; Shaw, 2006). The secondary structures are possibly oblique thrusts and folds formed in a transpressive regime during the southern propagation of the San Andreas Fault (e.g. Perrin et al., 2016; Titus et al., 2011 and references therein). Their obliquity varies depending on the distance from the main San Andreas Fault (Titus et al., 2011) and some of them could be still potentially active (ex: the 1983, Mw 6.2 Coalinga thrust earthquake, Stein and King, 1984, Mw 6.1 Kettleman Hills thrust earthquake, Ekström et al., 1992). The diffuse seismicity around Middle Mountain (Figs. 1, 2, S1, S4 and S5) might be explained by the presence of these secondary faults in the crustal medium surrounding the main San Andreas Fault. Yet, it seems unlikely that the presence of the stuck patch randomly coincides or results from the presence of the structural complexities. The San Andreas fault is a large cumulative slip fault with a very smooth (i.e., linear) surface fault trace along the central section (Wesnousky, 1988), except at the tips of the Parkfield section. Thus, it is necessary to find another mechanism responsible for the local twist of the fault plane. We propose a second, more likely, hypothesis: the local structural complexities were lately formed by the torque of the fault plane due to the presence of a locked fault patch surrounded by creeping zones at depth. Thus, secondary geological fault traces at MM and GH-CH should be considered in the common view of the active fault traces in California. They reflect the stress concentrations at the tip of the stuck patch at depth but can also enhance them. The geometrical complexities are marked by a wider distribution of the seismicity (Fig. 2d and Supplementary Fig. S4 and S5), associated with a deflection of the San Andreas fault plane (Fig. 8 and Supplementary Fig. S6). Finally, the flower structure shape highlighted in our model (Fig. 6b) is in good agreement with the development of secondary structures at depth that widen towards the surface (Fig. 1d and Supplementary Fig. S6).

4.1.3. Interpretations and numerical modeling of the twist at Parkfield: strengths and limitations

Simpson et al. (2006), using geological and geodetical observations in addition to the 2004 aftershock locations of Thurber et al. (2006), interpreted a deflection of the active San Andreas fault near GH-CH along the vertical axis in the upper ~6 km from its surface expression as the result of non-elastic behavior of upper crustal rock units. Our observation of a systematic change in fault dip along the entire Parkfield section from MM to GH-CH suggests an additional torque along the horizontal axis that causes the helicoidal nature of the three-dimensional fault plane, as shown in our model (Fig. 6). This shape is not predicted by the 2D numerical model in Simpson et al. (2006), which considers a constant, near-vertical dip at depth to obtain a warp in the fault plane with a major deflection at GH-CH, but not at MM. They suggest that the warp is due to slip in the creeping zone (including the Parkfield stuck patch), which results in inelastic deformation that is not released further to the south by large events similar to the 1857 earthquake. Our model of the helicoidal twist is based on the long-term difference in strength between persistent structures that represent stuck and creeping areas, and hence does not require inelasticity with such a short time constant.

The high friction patch (μ ~0.6) is velocity weakening and so exhibits an earthquake cycle. It is embedded in a region of low friction (μ ~0.2) which continuously slides in a stable manner. This strength contrast will place a clockwise torque on the system which by slow inelastic deformation over geologic time has twisted the fault. In this regard, our numerical models serve only two purposes: i) to demonstrate that the clockwise torque can arise from the assumed contrast in frictional strength along the Parkfield section and ii) to show that the clockwise torque can be sustained over many earthquake cycles on the high-friction patch.

In our model, the shear stress magnitude is significant (~100 MPa) and the correspondence principle between the linear elastic and the linear viscoelastic strain implies, over the long term, that our model's strain field could induce the development of permanent inelastic deformation in the upper part of the crust. This deformation might correspond to the secondary faults and fractures observed at surface and at depth at the tips of the stuck patch. More sophisticated fault and material models would be needed to investigate a causal relationship between the helicoidal twist of the stuck patch and the formation of secondary structures.

Our model indicates lateral deformation of the San Andreas fault of 1.5 m to 2 m at MM and 1.3 m to 2.5 m at GH (at surface and at depth, respectively) after 160 m of cumulative slip. Considering the current total cumulative slip around Parkfield since the fault initiation (i.e. ~315 km; Crowell, 1979; Revenaugh and Reasoner, 1997 and references therein), it would imply a total northeastern fault deformation of ~3 to ~4 km and ~2.5 to ~5 km at MM and GH, respectively. While this deformation is comparable observations at GH (~2 km wide step-over at the surface), it is not the case at MM. However, we note that our model has exaggerated contrast in friction strength between the patch and the creeping section. Increasing the friction coefficient of the creeping section to 0.2, compared to 0.1 used here, would possibly subdue the amount of the northeastern fault deformation. In addition, our model does not include the development of new secondary faults and fractures, which may have been created in the surrounding medium to accommodate the deflection of the San Andreas fault, just like the ~5 km wide zone of deformation identified at MM (see Fig. 1 and Thayer, 2006). Additional minor faults might be also present but they have been possibly eroded or hidden under sedimentary deposits.

Finally, we remind that our model is a simplified view that cannot exactly reproduce the deformation pattern of the San Andreas fault at Parkfield. The results are sensitive to the initial conditions
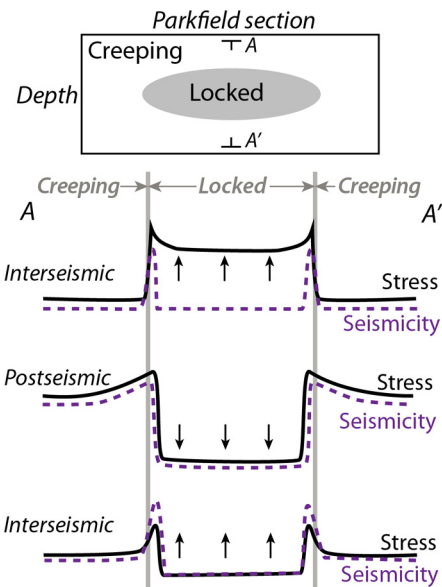

Fig. 9. Sketch showing a simplified view of the Parkfield fault section and along dip distribution of stress and seismicity rates (profile AA′) as predicted from a locked patch at mid-crustal depth imbedded in an otherwise creeping fault. Seismic activity is driven by the difference in the stress rate at the edge of the locked patch at every stage of the earthquake cycle.

(i.e. relative location of the stuck patch at depth and connection with the locked section in the south). For instance, we assume a vertical initial fault dip and the model does not reproduce the NE dip of the fault in the creeping section (Fig. 2c). On the other hand, we are not sure that this dip is related to the torque of the fault plane due to the presence of the stuck patch or rather to the initial fault dip of the San Andreas fault. All these parameters were not explored in this study and need to be tested in future models. Our model is used here to show that the right lateral motion and the change in fault sip behavior due to the presence of the stuck patch are in good agreement with the torque highlighted in our observations. The resulting stress and displacement values should be used with caution.

4.2. Impact of fault structures on the seismicity behavior and the earthquake cycle

Our results confirm that major structural discontinuities, such as secondary reverse and normal faults, are present at the surface near the transitions between the Parkfield and creeping sections at MM, and the Parkfield and Cholame sections near GH-CH (Fig. 1). Fine-scale analysis of the seismicity indicates that these structural complexities extend at depth and correlate with the vertices of the elliptical stuck patch that ruptures in M6 events (Figs. 2 and 3). It is recognized that aftershocks occur mostly at the edges of regions experiencing high coseismic slip or in areas of low coseismic slip (e.g., Mendoza and Hartzell, 1988), regardless of initial stress conditions. Along the Parkfield section, earthquake locations in both the post-seismic and interseismic periods over one and a half seismic cycles delineate the margins of the stuck patch (i.e. transition between locked and creeping areas on the fault; Figs. 2 and 3). Especially, Fig. 3d updates the common view of the "stationary" seismicity around the stuck patch, going through a new interseismic period, during the decade following the 2004 earthquake. Therefore, our observations indicate that the stress concentrations that surround the stuck patch and therefore the stuck patch itself are long-term permanent features controlling the rupture process.

Based on the results from our model (Fig. 7), we schematize in Fig. 9 the state of stress and seismicity distribution on the fault

plane. The seismicity distribution reflects significant stress concentrations between creeping regions, which are velocity strengthening and hence frictionally stable, and the locked region (i.e. stuck patch), which is velocity weakening and hence unstable. During interseismic periods (stage 1 in Fig. 9), the stress increases on the stuck patch relative to the surrounding creeping regions and higher stress concentrations are localized at the edge of the stuck patch. The resulting stress concentrations lead to higher seismic activity at the transition between locked and creeping regions. Coseismic slip produces surrounding stress concentrations during the postseismic period (stage 2 in Fig. 9) which also induces enhanced seismicity in that area. Then, the stress accumulates again along the locked section during the following interseismic period (stage 3 in Fig. 9), producing a similar behavior as in stage 1.

Our model shows that the long-term deformation of the fault plane is prominent at the along-strike extremities of the stuck patch (Figs. 5 and 6), leading to a concentration of stress and strain that can affect the seismic cycle. These zones also correspond to the nucleation locations of the 1934, 1966, and 2004 earthquakes (Bakun et al., 2005; Bakun and McEvilly, 1979). This behavior is also expected from results of dynamic modeling (Das and Kostrov, 1985) of rupture of an elliptical asperity, where the stress concentrations reach a maximum at the vertices of the semi-major axes of the ellipse. The rupture terminates shortly after it impinges on the velocity-strengthening region. This constitutes a stability barrier, as demonstrated by Kaneko et al. (2010). However, recent studies (Noda and Lapusta, 2013) show that some earthquake ruptures might also propagate through creeping areas that were considered to be barriers. The similarity of slip distribution of Parkfield earthquakes seems to suggest that the creeping zones stop rupture propagation at least for M6 and smaller earthquakes. The observation of logarithmically decaying afterslip sequences in the creeping section above the stuck patch following both the 1966 and 2004 earthquakes (e.g. Barbot et al., 2009; Langbein et al., 2006; Murray and Langbein, 2006; Scholz et al., 1969) is consistent with the model of Marone et al. (1991), in which a velocity strengthening region overlies a velocity weakening one.

5. Conclusions

We present a model based on geological surface observations and seismological observations at depth in which the three-dimensional structural complexities near MM and GH of the San Andreas Fault originate from the presence of a stuck patch surrounded by a creeping zone at Parkfield. The progressive helicoidal twist of the fault plane is due to a torque arising from the contrast in frictional strength between the stuck patch and the surrounding weak creeping area. The complex structures at each end of the helicoid result from the stress concentrations at these locations. They are characterized by complex reverse and normal faulting at the surface and diffuse seismicity at depth. These structural complexities are permanent features, playing an important role in stress concentrations and occurrence of M6 earthquakes at Parkfield.

Faults are laterally segmented along their traces. In the early stages of their evolution, the fault segments are separated by geometrical discontinuities possibly formed by small secondary faults and fractures As the fault grows and lengthens through time, fault segments tend to become more and more connected and the lateral discontinuities in between smoothed out (e.g. Manighetti et al., 2015 and references therein). The main strand of the San Andreas fault at Parkfield is extraordinarily smooth, as a result of its large cumulative slip (Wesnousky, 1988); the 2-km fault offset at GH-CH being a notable exception. We find that this offset is a constructive edifice resulting in the strength contrast in the fault at this locality. This example of fault roughening with slip is in contrast to the generally assumed smoothing of fully locked faults at they become more mature.

Appendix A. Supplementary material

Supplementary material related to this article can be found online at https://doi.org/10.1016/j.epsl.2019.06.010.

References

Aagaard, B.T., Knepley, M.G., Williams, C.A., 2016. PyLith user manual, version 2.1.2 [WWW document]. Comput. Infrastruct. Geodyn. http://geodynamics.org/cig/software/github/pylith/v2.1.2/pylith-2.1.2_manual.pdf.

Aagaard, B.T., Knepley, M.G., Williams, C.A., 2013. A domain decomposition approach to implementing fault slip in finite-element models of quasi-static and dynamic crustal deformation. J. Geophys. Res., Solid Earth 118, 3059–3079. https://doi.org/10.1002/jgrb.50217.

Aki, K., 1979. Characterization of barriers on an earthquake fault. J. Geophys. Res. 84, 6140–6148.

Allen, C.R., 1968. The tectonic environments of seismically active and inactive areas along the San Andreas fault system. Stanford Univ. Publ. Geol. Sci. 11.

Archuleta, R.J., Day, S.M., 1980. Dynamic rupture in a layered medium: the 1966 Parkfield earthquake. Bull. Seismol. Soc. Am. 70, 671–689.

Bakun, W.H., Aagaard, B., Dost, B., Ellsworth, W.L., Hardebeck, J.L., Harris, R.A., Ji, C., Johnston, M.J.S., Langbein, J., Lienkaemper, J.J., Michael, A.J., Murray, J.R., Nadeau, R.M., Reasenberg, P.A., Reichle, M.S., Roeloffs, E.A., Shakal, A., Simpson, R.W., Waldhauser, F., 2005. Implications for prediction and hazard assessment from the 2004 Parkfield earthquake. Nature 437, 969–974. https://doi.org/10.1038/nature04067.

Bakun, W.H., McEvilly, T.V., 1979. Earthquakes near Parkfield, California: comparing the 1934 and 1966 sequences. Science 205, 1375–1377. https://doi.org/10.1126/science.205.4413.1375.

Barbot, S., Fialko, Y., Bock, Y., 2009. Postseismic deformation due to the Mw 6.0 2004 Parkfield earthquake: stress-driven creep on a fault with spatially variable rate-and-state friction parameters. J. Geophys. Res., Solid Earth 114, 0-26. https://doi.org/10.1029/2008JB005748.

Barbot, S., Lapusta, N., Avouac, J.-P., 2012. Under the hood of the earthquake machine: toward predictive modeling. Science 80 (336), 707–710. https://doi.org/10.1126/science.1218796.

Barka, A., Kadinsky-Cade, K., 1988. Strike-slip fault geometry in Turkey. Tectonics 7, 663–684. https://doi.org/10.1029/TC007i003p00663.

Biasi, G.P., Wesnousky, S.G., 2017. Bends and ends of surface ruptures. Bull. Seismol. Soc. Am., 1–18. https://doi.org/10.1785/0120160292.

Brown, R.D.J., Vedder, J.G., Wallace, R.E., Roth, E.F., Yerkes, R.F., Castle, R.O., Waananen, A.O., Page, R.W., Eaton, J.P., 1967. The Parkfield-Cholame, California, earthquakes of June–August 1966 – surface geologic effects, water-resources aspects, and preliminary seismic data. U. S. Geol. Surv. Prof. Pap. 66.

Bruhat, L., Barbot, S., Avouac, J.-P., 2011. Evidence for postseismic deformation of the lower crust following the 2004 Mw6.0 Parkfield earthquake. J. Geophys. Res., Solid Earth 116, 1–10. https://doi.org/10.1029/2010JB008073.

Carpenter, B.M., Saffer, D.M., Marone, C., 2015. Frictional properties of the active San Andreas Fault at SAFOD: implications for fault strength and slip behavior. J. Geophys. Res., Solid Earth 120, 5273–5289. https://doi.org/10.1002/2015JB011963.

Crowell, J.C., 1979. The San Andreas fault system through time. J. Geol. Soc. Lond. 136, 293–302. https://doi.org/10.1144/gsjgs.136.3.0293.

Das, S., Kostrov, B.V., 1985. An elliptical asperity in shear: fracture process and seismic radiation. Geophys. J. Int. 80, 725–742. https://doi.org/10.1111/j.1365-246X.1985.tb05121.x.

Eaton, J.P., O'Neill, M.E., Murdock, J.N., 1970. Aftershocks of the 1966 Parkfield-Cholame, California, earthquake: a detailed study. Bull. Seismol. Soc. Am. 60, 1151–1197.

Ekström, G., Stein, R.S., Eaton, J.P., Eberhart-Phillips, D., 1992. Seismicity and geometry of a 110-km-long blind thrust fault 2. Synthesis of the 1982–1985 California Earthquake Sequence. J. Geophys. Res. 97, 4843–4864. https://doi.org/10.1029/91JB02847.

Hardebeck, J.L., 2010. Seismotectonics and fault structure of the California Central Coast. Bull. Seismol. Soc. Am. 100, 1031–1050. https://doi.org/10.1785/0120090307.

Harris, R.A., Segall, P., 1987. Detection of a locked zone at depth on the Parkfield, California, segment of the San Andreas Fault. J. Geophys. Res. 92, 7945–7962. https://doi.org/10.1029/JB092iB08p07945.

Irwin, W.P., Barnes, I., 1975. Effects of geological structure and metamorphic fluids on seismic behavior of the San Andreas fault system in central and northern California. Geology 3, 713–716.

Johanson, I.A., Fielding, E.J., Rolandone, F., Bürgmann, R., 2006. Coseismic and post-seismic slip of the 2004 Parkfield earthquake from space-geodetic data. Bull. Seismol. Soc. Am. 96, 269–282. https://doi.org/10.1785/0120050818.

Kaneko, Y., Avouac, J.-P., Lapusta, N., 2010. Towards inferring earthquake patterns from geodetic observations of interseismic coupling. Nat. Geosci. 3, 363–369. https://doi.org/10.1038/ngeo843.

Kim, W., Hong, T.-K., Lee, J., Taira, T., 2016. Seismicity and fault geometry of the San Andreas fault around Parkfield, California and their implications. Tectonophysics 677–678, 34–44. https://doi.org/10.1016/j.tecto.2016.03.038.

Langbein, J., Borcherdt, R., Dreger, D., Fletcher, J., Hardebeck, J.L., Hellweg, M., Ji, C., Johnston, M., Murray, J.R., Nadeau, R., Rymer, M.J., Treiman, J.a., 2005. Preliminary report on the 28 September 2004, M 6.0 Parkfield, California earthquake. Seismol. Res. Lett. 76, 10–26. https://doi.org/10.1785/gssrl.76.1.10.

Langbein, J., Murray, J.R., Snyder, H.A., 2006. Coseismic and initial postseismic deformation from the 2004 Parkfield, California, earthquake, observed by global positioning system, electronic distance meter, creepmeters, and borehole strainmeters. Bull. Seismol. Soc. Am. 96, 304–320. https://doi.org/10.1785/0120050823.

LeMaitre, J., 2001. Handbook of Materials Behavior Models. Academic Press.

Lindh, A.G., Boore, D.M., 1981. Control of rupture by fault geometry during the 1966 Parkfield earthquake. Bull. Seismol. Soc. Am. 71, 95–116.

Lockner, D.A., Morrow, C., Moore, D., Hickman, S., 2011. Low strength of deep San Andreas fault gouge from SAFOD core. Nature 472, 82–85. https://doi.org/10.1038/nature09927.

Lomax, A., Virieux, J., Volant, P., Berge, C., 2000. Probabilistic earthquake location in 3D and layered models: introduction of a Metropolis-Gibbs method and comparison with linear locations. In: Thurber, C.H., Rabinowitz, N. (Eds.), Advances in Seismic Event Location, pp. 101–134. Amsterdam.

Manighetti, I., Campillo, M., Bouley, S., Cotton, F., 2007. Earthquake scaling, fault segmentation, and structural maturity. Earth Planet. Sci. Lett. 253, 429–438. https://doi.org/10.1016/j.epsl.2006.11.004.

Manighetti, I., Caulet, C., De Barros, D., Perrin, C., Cappa, F., Gaudemer, Y., 2015. Generic along-strike segmentation of Afar normal faults, East Africa: implications on fault growth and stress heterogeneity on seismogenic fault planes. Geochem. Geophys. Geosyst. 16, 443–467. https://doi.org/10.1002/2014GC005691.Received.

Marone, C.J., Scholz, C.H., Bilham, R., 1991. On the mechanics of earthquake afterslip. J. Geophys. Res. 96, 8441. https://doi.org/10.1029/91JB00275.

McEvilly, T.V., Bakun, W.H., Casaday, K.B., 1967. The Parkfield, California, earthquakes of 1966. Bull. Seismol. Soc. Am. 57, 1221–1244.

Mendoza, C., Hartzell, S.H., 1988. Aftershock patterns and main shock faulting. Bull. Seismol. Soc. Am. 78, 1438–1449.

Moore, D.E., Lockner, D.A., 2013. Chemical controls on fault behavior: weakening of serpentinite sheared against quartz-bearing rocks and its significance for fault creep in the San Andreas system. J. Geophys. Res., Solid Earth 118, 2558–2570. https://doi.org/10.1002/jgrb.50140.

Moore, D.E., Lockner, D.A., Hickman, S., 2016. Hydrothermal frictional strengths of rock and mineral samples relevant to the creeping section of the San Andreas Fault. J. Struct. Geol. 89, 153–167. https://doi.org/10.1016/j.jsg.2016.06.005.

Moore, D.E., Rymer, M.J., 2007. Talc-bearing serpentinite and the creeping section of the San Andreas fault. Nature 448, 795–797. https://doi.org/10.1038/nature06064.

Murray, J., Langbein, J., 2006. Slip on the San Andreas fault at Parkfield, California, over two earthquake cycles, and the implications for seismic hazard. Bull. Seismol. Soc. Am. 96, 283–303. https://doi.org/10.1785/0120050820.

Noda, H., Lapusta, N., 2013. Stable creeping fault segments can become destructive as a result of dynamic weakening. Nature 493, 518–521. https://doi.org/10.1038/nature11703.

Perrin, C., Manighetti, I., Gaudemer, Y., 2016. Off-fault tip splay networks: a genetic and generic property of faults indicative of their long-term propagation. C. R. Géosci. 348, 52–60. https://doi.org/10.1016/j.crte.2015.05.002.

Revenaugh, J., Reasoner, C., 1997. Cumulative offset of the San Andreas fault in central California: a seismic approach. Geology 25, 123–126. https://doi.org/10.1130/0091-7613(1997)025<0123:COOTSA>2.3.CO;2.

Rymer, M.J., Tinsley, J.C., Treiman, J.A., Arrowsmith, J.R., Ciahan, K.B., Rosinski, A.M., Bryant, W.A., Snyder, H.A., Fuis, G.S., Toké, N.A., Bawden, G.W., 2006. Surface fault slip associated with the 2004 Parkfield, California, earthquake. Bull. Seismol. Soc. Am. 96, 11–27. https://doi.org/10.1785/0120050830.

Schaff, D.P., Waldhauser, F., 2005. Waveform cross-correlation-based differential travel-time measurements at the northern California seismic network. Bull. Seismol. Soc. Am. 95, 2446–2461. https://doi.org/10.1785/0120040221.

Scholz, C.H., Wyss, M., Smith, S.W., 1969. Seismic and aseismic slip on the San Andreas Fault. J. Geophys. Res. 74, 2049–2069. https://doi.org/10.1029/JB074i008p02049.

Segall, P., Du, Y., 1993. How similar were the 1934 and 1966 Parkfield earthquakes? J. Geophys. Res. 98, 4527–4538. https://doi.org/10.1029/92JB02408.

Shaw, B.E., 2006. Initiation propagation and termination of elastodynamic ruptures associated with segmentation of faults and shaking hazard. J. Geophys. Res. 111, B08302. https://doi.org/10.1029/2005JB004093.

Simpson, R.W., Barall, M., Langbein, J., Murray, J.R., Rymer, M.J., 2006. San Andreas fault geometry in the Parkfield, California, region. Bull. Seismol. Soc. Am. 96, 28–37. https://doi.org/10.1785/0120050824.

Stein, R.S., King, G.C.P., 1984. Seismic potential revealed by surface folding: 1983 Coalinga, California, earthquake. Science 80 (224), 869–872.

Stirling, M.W., Wesnousky, S.G., Shimazaki, K., 1996. Fault trace complexity, cumulative slip, and the shape of the magnitude-frequency distribution for strike-slip faults: a global survey. Geophys. J. Int. 124, 833–868. https://doi.org/10.1111/j.1365-246X.1996.tb05641.x.

Thayer, M., 2006. Structural Geology of the San Andreas Fault Zone at Middle Mountain, Near Parkfield, Central California. Doctoral Dissertation. Arizona State University.

Thurber, C., Zhang, H., Waldhauser, F., Hardebeck, J.L., Michael, A.J., Eberhart-Phillips, D., 2006. Three-dimensional compressional wavespeed model, earthquake relocations, and focal mechanisms for the Parkfield, California, region. Bull. Seismol. Soc. Am. 96, S38–S49. https://doi.org/10.1785/0120050825.

Titus, S.J., Dyson, M., DeMets, C., Tikoff, B., Rolandone, F., Bürgmann, R., 2011. Geologic versus geodetic deformation adjacent to the San Andreas fault, central California. Bull. Geol. Soc. Am. 123, 794–820. https://doi.org/10.1130/B30150.1.

U.S. Geological Survey and California Geological Survey, 2006. Quaternary fault and fold database for the United States [WWW document]. https://earthquake.usgs.gov/hazards/qfaults/. (Accessed 10 February 2014).

Uhrhammer, R.A., Hellweg, M., Hutton, K., Lombard, P., Walters, A.W., Hauksson, E., Oppenheimer, D., 2011. California integrated seismic network (CISN) local magnitude determination in California and vicinity. Bull. Seismol. Soc. Am. 101, 2685–2693. https://doi.org/10.1785/0120100106.

Waldhauser, F., 2001. HypoDD: a Computer Program to Compute Double-Difference Hypocenter Locations. U.S. Geol. Surv. Open File Rep. 01-113. U.S. Geol. Surv., Menlo Park, Calif. 25.

Waldhauser, F., Ellsworth, W.L., 2000. A Double-difference Earthquake location algorithm: method and application to the Northern Hayward Fault, California. Bull. Seismol. Soc. Am. 90, 1353–1368. https://doi.org/10.1785/0120000006.

Waldhauser, F., Ellsworth, W.L., Schaff, D.P., Cole, A., 2004. Streaks, multiplets, and holes: high-resolution spatio-temporal behavior of Parkfield seismicity. Geophys. Res. Lett. 31, L18608. https://doi.org/10.1029/2004GL020649.

Waldhauser, F., Schaff, D.P., 2008. Large-scale relocation of two decades of Northern California seismicity using cross-correlation and double-difference methods. J. Geophys. Res., Solid Earth 113, 1–15. https://doi.org/10.1029/2007JB005479.

Wesnousky, S.G., 1988. Seismological and structural evolution of strike-slip faults. Nature. https://doi.org/10.1038/335340a0.